# Three-axis magnetic field detection with a compact, high-bandwidth, single beam zero-field atomic magnetometer

Rach Dawson[a], Carolyn O'Dwyer[a], Marcin S. Mrozowski[a], Stuart Ingleby[a], Paul. F. Griffin[a], and Erling Riis[a]

[a]Department of Physics, SUPA, University of Strathclyde, Glasgow G4 0NG, United Kingdom

## ABSTRACT

Zero-field optically pumped magnetometers (OPMs) have emerged as an important technology in the realm of biomagnetic research, providing extremely small magnetic field detection capabilities, femtotesla-level, contained in a non-cryogenic compact form factor. Often, compact zero-field OPMs extract single or two-axis magnetic information, typically with a sensing bandwidth of $< 100$ Hz. The resolution of multiple axes of magnetic field is particularly important for accurate representation of radial components of biomagnetic fields. However, the presence of multi-axis static magnetic fields across the OPM causes measurement errors that degrade signal resolution.[1] Here, we utilise our compact caesium single beam zero-field OPM[2] to address these limitations. We magnetically modulated along both transverse axes of the sensor, at unique frequencies, to extract all axes static-field information. Active feedback can be realised through a lock-in detection scheme at $f_{\mathrm{Mod},x/y}$ for the $x$- and $y$-axes, and at $2f_{\mathrm{Mod},x}$ for the beam axis, $z$. Operation in this scheme allows for the extraction of three-axis magnetic field information from only a single beam and highlights the importance of active feedback in high-sensitivity biomagnetic applications. The portable sensor also demonstrates a bandwidth with a -3 dB point at $\simeq 1600$ Hz. The combination of high bandwidth and the capability to extract three-axis magnetic fields opens up exciting prospects for resolving high-frequency biomagnetic signals.

**Keywords:** SERF, OPM, three-axis detection, vectorisation, high-bandwidth

## 1. INTRODUCTION

Magnetic field measurements of the human body are essential for diagnostics and research.[3–10] Advances in optically pumped magnetometers (OPMs)[11–14] have led to demonstrations of sensors that approach the sensitivity of low-temperature superconducting quantum interference devices (SQUIDs), without the need for cryogenics, lending themselves to mobile or functional measurements. Zero-field OPMs are pivotal in biomagnetism due to sensitivity ($10^{-15}$ T level), size and portability capabilities, which may combine to facilitate new biomagnetic measurement paradigms.[15] Portability is critical in enabling multiple sensors to be utilised simultaneously in arrays to provide spatial information for biomagnetic measurements, as demonstrated for full head magnetoencephalography (MEG)[16,17] and full chest magnetocardiography (MCG).[18] Developments in portable zero-field OPMs have improved source localisation[19] due to better signal coverage,[16,20,21] where the measurement of accurate magnetic field information underpins the accurate extraction of spatial and temporal information.

OPMs utilise laser light to optically pump an atomic ensemble of alkali vapour into a polarised atomic state, and optically probe the ensemble to measure the atomic response to a magnetic field. In the interest of miniaturisation and portability, zero-field OPMs for biomagnetic measurements typically utilise a single laser beam to both pump and probe,[22,23] however, such schemes are typically demonstrated for single[24] or dual axis magnetic field information.

Three-axis magnetic field extraction schemes for zero-field OPM have been proposed for dual[25,26] and single beam[22,23,27] OPM configurations to promising effect. However, these schemes require a considerable increase in the complexity of the sensor design or operation. Here, we propose a three-axis single beam OPM detection scheme based on only two cross-modulating fields. By extracting magnetic information across all three axes from a single beam, we aim to maintain zero-field across the atomic ensemble at all times. This prevents any systematic measurement error to arise that is caused by the presence of multi-axis magnetic fields perpendicular to the sensitive axis of an OPM,[1] to more accurately measure components of an applied magnetic field.

Quantum Sensing, Imaging, and Precision Metrology II, edited by Jacob Scheuer, Selim M. Shahriar, Proc. of SPIE Vol. 12912, 1291210 · © 2024
SPIE · 0277-786X · doi: 10.1117/12.3002678

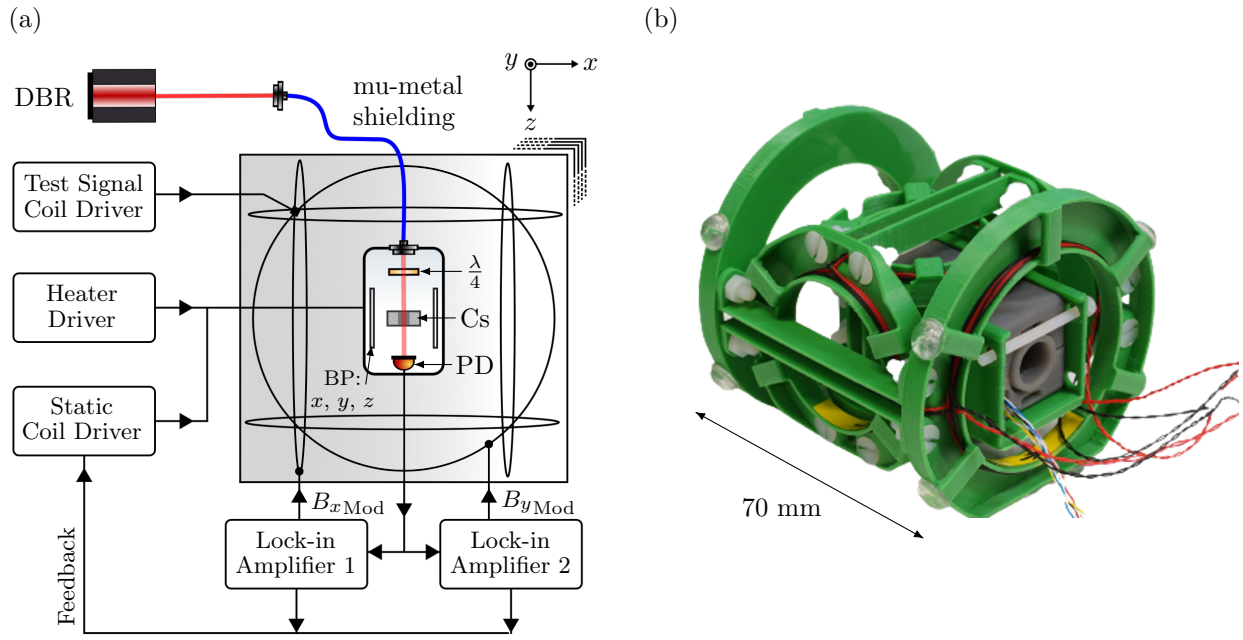


Figure 1. **a**) Setup of the portable caesium (Cs) zero-field magnetometer. The sensor head operates inside a five-layer mu-metal shield. The laser light from the Distributed Bragg Reflector (DBR) is delivered to the sensor-head using an optical fibre. Bi-planar coils (BP) inside the sensor-head provide three-axis static field control.[2] The driving and control electronics including Data Acquisition (DAQ) unit, coil driver,[34] lock-in amplifiers and cell heater driver operate outside the shielding. **b**) Photograph of the portable caesium zero-field magnetometer within multiple pairs of Helmholtz coils wound on 3D printed coil formers.

## 2. EXPERIMENTAL SETUP

The setup of the portable caesium zero-field magnetometer is shown in Fig. 1, as detailed fully in,[2] here housed within a laboratory setting. The micro-fabricated atomic vapour cell[28] containing caesium atoms and 225 Torr of nitrogen buffer gas is heated to $\simeq$ 120 °C by AC resistive heating, to reach the atomic density required to reach the spin-exchange relaxation free regime.[29] In this regime, spin-exchange collisions no longer cause spin relaxation because the entire alkali ensemble precesses coherently,[29–31] facilitating high-sensitivity measurements. To attenuate any magnetic fields present in our laboratory environment, the sensor is housed in a 5-layer mu-metal shield, with a shielding factor of $\simeq$ $10^5$, creating a low nT-level magnetic field environment across the sensing atoms. The shield's internal residual magnetic field is effectively neutralised through the implementation of three pairs of bi-planar coils, offering three-axis orthogonal field control within the sensor package.[2] Multiple Helmholtz-like coils are also utilised, where the resulting magnetic field is easily calculated through derivation of the Biot-Savart law.[32,33] Three pairs of orthogonal Helmholtz coils located outside the sensor package are used to apply magnetic test signals. The static fields are driven using a custom low-noise current driver.[34] A further two sets of Helmholtz coils are used to modulate the magnetic field across the $x$- and $y$-axes, $B_{x_{\mathrm{Mod}}}$ and $B_{y_{\mathrm{Mod}}}$ respectively. The atoms are pumped along the $z$ direction by a 6 mW Distributed Bragg Reflector (DBR) laser tuned to the $D_1$ resonance of caesium close to the $F = 4 \rightarrow F' = 3$ hyperfine transition. The laser light is elliptically polarised through the use of a $\frac{\lambda}{4}$ waveplate, to facilitate optimal optical pumping and probing[35] of the atomic vapour, and is then incident on a photodiode to measure light transmission through the vapour cell.

## 3. THREE-AXIS OPERATION

The practical three-axis operation of the OPM first requires multi-axis calibration to ascertain the magnetic field that corresponds to any change in the measured photodiode voltage. The sensor calibration procedure utilises the Hanle effect, the response of laser light transmission through an atomic ensemble under the influence of a close-to-zero magnetic field,[36] to identify the zero-field point across each axis, $B_{x0}$, $B_{y0}$, and $B_{z0}$. These field

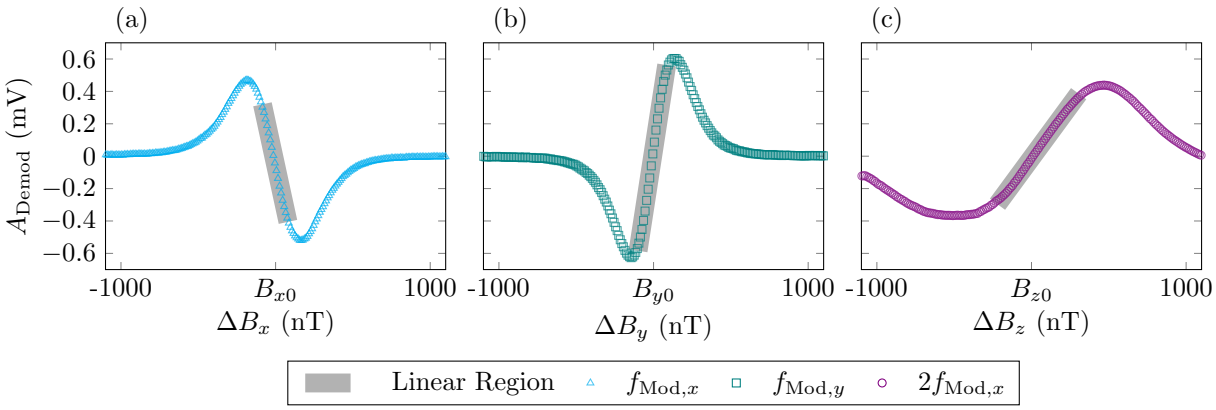


Figure 2. Lock-in features for the **a)** $x-$, **b)** $y-$ and **c)** $z-$axes, extracted from the amplitude of the demodulated response, $A_{\mathrm{Demod}}$, measured with respect to a sweeping magnetic field applied along the corresponding axis. Colour indicates the frequency of demodulation which occurs at $f_{\mathrm{Mod},x/y}$ for the $x$- and $y$-axes, and at $2f_{\mathrm{Mod},x}$ for the beam axis, $z$. The grey shaded areas indicate the linear response region, in which the atomic response to magnetic field is linear. $B_{x0}$, $B_{y0}$ and $B_{z0}$ indicate the zero-field point for the $x-$, $y-$ and $z-$axis respectively.

values are applied using the internal biplanar coils within the sensor package to maintain a zero-field environment, as described fully in.[37] Once the static residual fields are cancelled, two modulating fields, $B_{x\mathrm{Mod}}$ and $B_{y\mathrm{Mod}}$ are applied along the corresponding axes at unique frequencies $f_{\mathrm{Mod},x}$ and $f_{\mathrm{Mod},y}$ respectively. The static fields across each axis are swept iteratively, and the resultant signal is demodulated, $A_{\mathrm{Demod}}$, using two lock-in amplifiers at $f_{\mathrm{Mod},x/y}$ for the transverse $x$- and $y$-axes, and $2f_{\mathrm{Mod},x}$ for the longitudinal $z$-axis, as seen in Table. [1]. By repeating at each value of applied field, a dispersive signal is obtained for each axis, shown in Fig. 2.

The demodulated dispersive signals, shown in Fig. 2, act as the foundation for three-axis lock-in detection at the zero-point. The linear response, indicated by the shaded regions, defines the dynamic range, $R_{dyn}$, in which the measured response of the signal is proportional to the applied magnetic field. Linearity is important for accurate sensing, to reliably provide the calibration of measured atomic response to a magnetic field value. The slope of the demodulated signal in the linear region around zero field, for each axis, provides the axis-specific signal-to-field conversion (mV/nT). Sensor calibration by this method ensures the field across the sensor is zeroed, and the system response in terms of signal to magnetic field, is accurate across all three axes. Table [1] shows the extracted slope and dynamic range for each axis, found using a simple linear model which in turn defines the linear region boundaries.

## 4. THREE-AXIS SENSITIVITY AND BANDWIDTH

The bandwidth and sensitivity of the sensor are characterised, as shown in Fig. 3. The bandwidth is extracted from the recovered amplitude of an applied 2 nT sine wave across the sensitive axis, for a logarithmic range of frequencies between 1 Hz and 40 kHz. The dashed line, in Fig. 3(b), indicates a 2nd order low-pass filter response fit to the measured data, with a -3 dB corner frequency of $\simeq$ 1600 Hz. The sensitivity along each axis,

Table 1. Definition of modulation amplitude, $A_{\mathrm{Mod}}$ and modulation frequency, $f_{\mathrm{Mod}}$, for each sensor axis. The linear response within the demodulated signal for each axis is used to extract the slope (mV/nT), where the dynamic range, $R_{dyn}$, defines the boundaries of the linear response. The sensitivity along each axis is directly measured by scaling the square root of the power spectral density of each axis by the slope and averaging across the 5 - 20 Hz frequency band.

| Axis | $A_{\mathrm{Mod}}$ (nT) | $f_{\mathrm{Mod}}$ (Hz) | $R_{dyn}$ (nT) | Slope (mV/nT) | Sensitivity (fT/$\sqrt{\mathrm{Hz}}$) |
|---|---|---|---|---|---|
| $x$ | 150 | 507 | ± 80 | 44 | 150 |
| $y$ | 220 | 721 | ± 90 | 62 | 94 |
| $z$ | - | - | ± 260 | 13 | 321 |

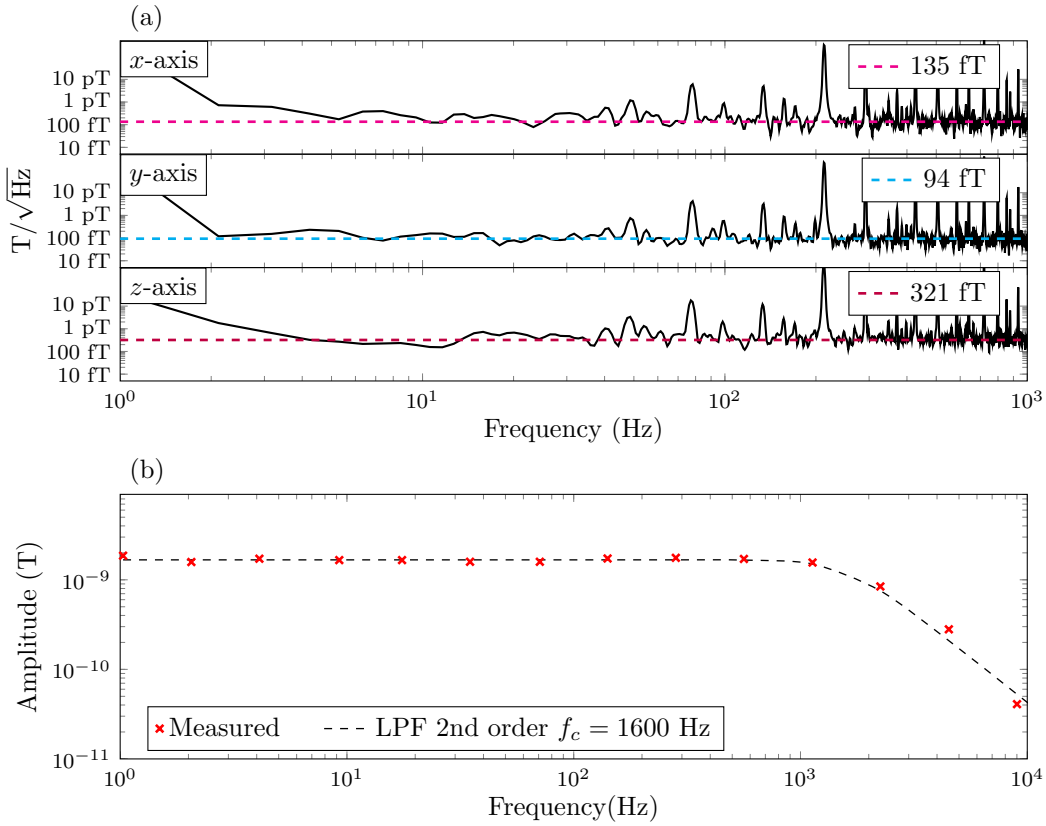


Figure 3. **a**) The measured magnetic noise floor of the sensor for each axis as labelled, the dashed line indicates the geometric mean calculated in the frequency band of interest (5-20 Hz). **b**) Measured bandwidth extracted through the recovery of the amplitude of an applied sine wave, applied at 2 nT magnitude, at various frequencies. The dashed line indicated a 2nd order low-pass filter fit to the measured data, with a corner frequency of $\simeq$ 1600 Hz.

Fig. 3(a), is directly measured by scaling the square root of the power spectral density of each axis by the slope and averaging across the 5-20 Hz frequency band.

## 5. DISCUSSION

Here we demonstrated and implemented the use of two, rather than three, axis modulation in a single beam zero-field OPM, to gather three-axis magnetic field information. There are distinct advantages to this method, in both the reduction of complexity for computation, and also by incurring fewer potential technical noise sources such as those introduced by driving currents for a third modulating field. We have shown that magnetic fields along the beam, $z$-axis, can be extracted from the atomic response demodulated at the second harmonic of the modulation on the $x$-axis, $2f_{\mathrm{Mod},x}$. However in future work we will fully explore demodulating at $f_{\mathrm{Mod},x/y}$ and $2f_{\mathrm{Mod},x/y}$ for both modulation axes, and all combinations there of, to optimise the extraction of the $z$-axis magnetic field information.

Using this technique the OPM has a demonstrated sub 400 fT/$\sqrt{\mathrm{Hz}}$ average sensitivity across the 5-20 Hz frequency band, for all axes, and sub 100 fT/$\sqrt{\mathrm{Hz}}$ on the most sensitive axis. This peak sensitivity, <100 fT/$\sqrt{\mathrm{Hz}}$, aligns with the expected sensitivity for caesium based OPMs in this configuration.[2] However, the authors are preparing a publication demonstrating this technique in a rubidium based OPM, with more competitive sensitivity capabilities.

Table [1] indicates a trade-off between the dynamic range of the sensor, in which the observed response to a field is linear, and sensitivity. The dynamic ranges across all axes allow the sensor to be situated in changing

fields in the 10's of nT range, whilst allowing resolution of biomagnetism level signals. The main limitation of this multi-axis modulation method is potential delays in response within a closed-loop feedback system due to sampling time, however, the wide observed bandwidth mitigates this.

## REFERENCES


[1] A. Borna, J. Iivanainen, T. R. Carter, *et al.*, "Cross-Axis projection error in optically pumped magnetometers and its implication for magnetoencephalography systems," *NeuroImage* **247**, 118818 (2022).

[2] R. Dawson, C. O'Dwyer, M. S. Mrozowski, *et al.*, "Portable single-beam cesium zero-field magnetometer for magnetocardiography," *Journal of Optical Microsystems* **3**, 044501 (2023).

[3] A. Meyer-Baese, S. I. Dimitriadis, P. K. Mandal, *et al.*, "A Comprehensive Review of Magnetoencephalography (MEG) Studies for Brain Functionality in Healthy Aging and Alzheimer's Disease (AD)," *Frontiers in Computational Neuroscience* **1**, 60 (2018).

[4] H. Kwon, K. Kim, Y. H. Lee, *et al.*, "Non-invasive magnetocardiography for the early diagnosis of coronary artery disease in patients presenting with acute chest pain," *Circulation Journal* **74**, 1424–30 (2010).

[5] Y. Chen and A. Zhan, "Clinical value of magnetic resonance imaging in identifying multiple cerebral gliomas from primary central nervous system lymphoma," *Oncology Letters* **18**, 593–598 (2019).

[6] J. Zhang, J. Xiang, L. Luo, *et al.*, "Editorial: EEG/MEG based diagnosis for psychiatric disorders," *Frontiers in Human Neuroscience* **16**, 1061176 (2022).

[7] N. Hamedi, A. Khadem, M. Delrobaei, *et al.*, "Detecting ADHD Based on Brain Functional Connectivity Using Resting-State MEG Signals," *Frontiers in Biomedical Technologies* **9**, 110–118 (2022).

[8] H. Hamada, H. Horigome, M. Asaka, *et al.*, "Prenatal diagnosis of long QT syndrome using fetal magnetocardiography," *Prenatal Diagnosis* **19**, 677–80 (1999).

[9] S. Watanabe and S. Yamada, "Magnetocardiography in Early Detection of Electromagnetic Abnormality in Ischemic Heart Disease," *Journal of Arrhythmia* **24**, 4–17 (2008).

[10] M. A. Lopes, D. Krzemiński, K. Hamandi, *et al.*, "A computational biomarker of juvenile myoclonic epilepsy from resting-state MEG," *Clinical Neurophysiology* **132**, 922–927 (2021).

[11] H. B. Dang, A. C. Maloof, and M. V. Romalis, "Ultrahigh sensitivity magnetic field and magnetization measurements with an atomic magnetometer," *Applied Physics Letters* **97**, 151110 (2010).

[12] J. C. Allred, R. N. Lyman, T. W. Kornack, *et al.*, "High-sensitivity atomic magnetometer unaffected by spin-exchange relaxation," *Physical Review Letters* **89**, 1308011–1308014 (2002).

[13] M. P. Ledbetter, I. M. Savukov, V. M. Acosta, *et al.*, "Spin-exchange-relaxation-free magnetometry with Cs vapor," *Physical Review A - Atomic, Molecular, and Optical Physics* **77**, 1–8 (2008).

[14] J. Fang, S. Wan, J. Qin, *et al.*, "Spin-exchange relaxation-free magnetic gradiometer with dual-beam and closed-loop Faraday modulation," *Journal of the Optical Society of America B* **31**, 512 (2014).

[15] M. J. Brookes, J. Leggett, M. Rea, *et al.*, "Magnetoencephalography with optically pumped magnetometers (OPM-MEG): the next generation of functional neuroimaging," (2022).

[16] M. Jas, S. R. Jones, and M. S. Hämäläinen, "Whole-head OPM-MEG enables noninvasive assessment of functional connectivity," *Trends in Neurosciences* **44**, 510–512 (2021).

[17] R. M. Hill, E. Boto, M. Rea, *et al.*, "Multi-channel whole-head OPM-MEG: Helmet design and a comparison with a conventional system," *NeuroImage* **219**, 116995 (2020).

[18] Y. Yang, M. Xu, A. Liang, *et al.*, "A new wearable multichannel magnetocardiogram system with a SERF atomic magnetometer array," *Scientific Reports* **11**, 5564 (2021).

[19] E. Boto, R. Bowtell, P. Krüger, *et al.*, "On the potential of a new generation of magnetometers for MEG: A beamformer simulation study," *PLoS ONE* **11**, e0157655 (2016).

[20] M. Rea, E. Boto, N. Holmes, *et al.*, "A 90-channel triaxial magnetoencephalography system using optically pumped magnetometers," *Annals of the New York Academy of Sciences* **1517**, 107–124 (2022).

[21] E. Boto, N. Holmes, J. Leggett, *et al.*, "Moving magnetoencephalography towards real-world applications with a wearable system," *Nature* **555**, 657–661 (2018).

[22] J. Tang, Y. Zhai, L. Cao, *et al.*, "High-sensitivity operation of a single-beam atomic magnetometer for three-axis magnetic field measurement," *Optics Express* **29**, 15641 (2021).

[23] H. Huang, H. Dong, and L. Chen, "Single-beam three-axis atomic magnetometer," *Appl. Phys. Lett* **109**, 62404 (2016).

[24] Y. Chen, , L. Zhao, *et al.*, "Single beam Cs-Ne SERF atomic magnetometer with the laser power differential method," *Optics Express* **30**, 16541–16552 (2022).

[25] S. J. Seltzer and M. V. Romalis, "Unshielded three-axis vector operation of a spin-exchange-relaxation-free atomic magnetometer," *Applied Physics Letters* **85**, 4804–4806 (2004).

[26] S. Zou, H. Zhang, X. yuan Chen, *et al.*, "In-situ triaxial residual magnetic field measurement based on optically-detected electron paramagnetic resonance of spin-polarized potassium," *Measurement* **187**, 110338 (2022).

[27] J. Fang and J. Qin, "In situ triaxial magnetic field compensation for the spin-exchange- relaxation-free atomic magnetometer," *Review of Scientific Instruments* **83**, 103104 (2012).

[28] S. Dyer, P. F. Griffin, A. S. Arnold, *et al.*, "Micro-machined deep silicon atomic vapor cells," *J. Appl. Phys* **132**, 134401 (2022).

[29] W. Happer and A. C. Tam, "Effect of rapid spin exchange on the magnetic-resonance spectrum of alkali vapors," *Physical Review A* **16**, 1877–1891 (1977).

[30] S. J. Seltzer, *Developments in Alkali-Metal Atomic Magnetometry*. PhD thesis, Princeton University, New Jersey (2008).

[31] I. Savukov and S. J. Seltzer, "Spin-exchange-relaxation-free (SERF) magnetometers," in *Optical Magnetometry*, D. Budker and D. F. Jackson Kimball, Eds., 85–103, Cambridge University Press, Cambridge (2013).

[32] R. Carter, "Coil-system design for production of uniform magnetic fields," *Proceedings of the Institution of Electrical Engineers* **123**, 1279 (1976).

[33] A. F. Restrepo, E. Franco, H. Cadavid, *et al.*, "A comparative study of the magnetic field homogeneity for circular, square and equilateral triangular helmholtz coils," *2017 International Conference on Electrical, Electronics, Communication, Computer, and Optimization Techniques (ICEECCOT)* **2018-January**, 13–20, IEEE (2017).

[34] M. S. Mrozowski, I. C. Chalmers, S. J. Ingleby, *et al.*, "Ultra-low noise, bi-polar, programmable current sources," *Review of Scientific Instruents* **94**, 1–9 (2023).

[35] V. Shah and M. V. Romalis, "Spin-exchange relaxation-free magnetometry using elliptically polarized light," *Physical Review A* **80**, 013416 (2009).

[36] N. Castagna and A. Weis, "Measurement of longitudinal and transverse spin relaxation rates using the ground-state Hanle effect," *Physical Review A - Atomic, Molecular, and Optical Physics* **84**, 1–11 (2011).

[37] R. Dawson, C. O'Dwyer, E. Irwin, *et al.*, "Automated Machine Learning Strategies for Multi-Parameter Optimisation of a Caesium-Based Portable Zero-Field Magnetometer," *Sensors* **23**, 4007 (2023).